Published in final edited form as:
Nature. 2019 February ; 566(7744): 350–353. doi:10.1038/s41586-019-0909-9.

A new inner moon of Neptune

M. R. Showalter[1], **I. de Pater**[2], **J. J. Lissauer**[3], and **R. S. French**[1]

[1]SETI Institute, 189 Bernardo Avenue, Suite 200, Mountain View, CA 94043, USA.

[2]Department of Astronomy, University of California, Berkeley, CA 94720, USA.

[3]NASA Ames Research Center, Moffett Field, CA 94035, USA.

Abstract

During its 1989 flyby, the Voyager 2 spacecraft imaged six small moons of Neptune, all orbiting well interior to the large, retrograde moon Triton[1]. Along with a set of nearby rings, these moons are probably younger than Neptune itself; they formed shortly after the capture of Triton and most of them have probably been fragmented multiple times by cometary impacts[1–3]. Here we report observations of a seventh inner moon, Hippocamp. It is smaller than the other six, with a mean radius $R \approx 17$ km. We also recover Naiad, Neptune's innermost moon, seen for the first time since 1989. We provide new astrometry, orbit determinations, and size estimates for all the inner moons. Hippocamp orbits close to Proteus, the outermost and largest of these moons; the fractional separation is only 10 percent. Proteus has migrated outward because of tidal interactions with Neptune. We suggest that Hippocamp is probably an ancient fragment of Proteus, providing further support for the hypothesis that the inner Neptune system has been shaped by numerous impacts.

We have devoted three HST observing programs to studies of the rings, ring-arcs, and small inner moons of Neptune. We used the High Resolution Channel (HRC) of the Advanced Camera for Surveys (ACS) in 2004–2005 and the Ultraviolet/Visual Imager (UVIS) of Wide Field Channel 3 (WFC3) in 2009 and 2016. Hippocamp, also designated S/2004 N 1[4] and Neptune XIV, was discovered during a reanalysis of the first two data sets (Figs. 1a–c) and confirmed in the third (Fig 1d).

The long delay between first image acquisition and the discovery arose because of the specialized image processing techniques required. To detect a small moon in an image, motion smear should be limited to the scale of the point spread function (PSF). For Neptune's inner system, this limits exposure times to 200–300 s before smear dominates and the signal-to-noise ratio (SNR) ceases to grow. We have developed an image processing

---

Author contributions MRS, IdP, and JJL are the co-investigators on the HST programs that led to the discovery of Hippocamp. MRS and RSF performed the data analysis and modeling effort. IdP provided additional data analysis methods that contributed to our interpretation of the results. JJL contributed the theoretical analysis and interpretation of the Neptune system's long-term evolution and the origin of Hippocamp. All authors contributed to the final version of the manuscript.

Correspondence and requests for materials should be addressed to MRS (mshowalter@seti.org).

The authors declare no competing interests.

technique to push integration times well beyond this limit. Although the moons of Neptune move rapidly across the detector, that motion is predictable and can be described by a distortion model. Our procedure is to derive a pair of functions $r(\mathbf{x})$ and $\theta(\mathbf{x})$, which return orbital radius and inertial longitude as a function of 2-D pixel coordinate $\mathbf{x}$. The inverse function $\mathbf{x}(r,\theta)$ can also be readily defined. We derive the mean motion function $n(r)$ from Neptune's gravity field including its higher moments J_2 and J_4[5]. One can use these functions to transform an image taken at time t_0 to match the appearance of another image at time t_1, by relocating each pixel $\mathbf{x}_0$ in the original image to a new location $\mathbf{x}_1$:

$$\mathbf{x}_1 = \mathbf{x}\left(r(\mathbf{x}_0), \theta(\mathbf{x}_0) + n(r(\mathbf{x}_0)) \times [t_1 - t_0]\right). \quad [1]$$

After the transformation, any moon on a prograde, circular, equatorial orbit will appear at fixed pixel coordinates. Transformed images can be coadded so that much longer effective exposure times are obtained (Fig. 2). The transformation creates a spiral pattern that winds tighter with decreasing r (Fig. 2c) and fails when adjacent pixels sheer to the point that individual PSFs are severely distorted. For the inner Neptune system, this limits the coadding of images to those that have been obtained within a single HST orbit of Earth, which typically allows 50 minutes of Neptune observing.

We have obtained 20 detections of Hippocamp (Extended Data Table 1). Most detections required coadding all of the 8–11 long exposures taken within most HST orbits. In 2016, by timing our orbits carefully relative to Hippocamp's orbit and by using the broadest filter (F350LP), we were consistently able to detect the moon in half-orbits comprising only ~ 15 minutes of integration. Detections vary in statistical significance from 2.3 to 13.2. Hippocamp is most detectable at maximum elongation, where sky motion is slower, background noise is reduced and, if the body is irregular, it presents a larger cross-section. A combination of favorable circumstances provided us with one visit in which Hippocamp was visible without coadding; see Supplementary Videos 1 and 2.

This same procedure has also revealed Naiad (Extended Data Fig. 1; Extended Data Table 2). Identifying Naiad was challenging because its orbit differed substantially from that predicted by the latest ephemeris[6]; in 2016, Naiad fell nearly 180 away from its predicted location. Nevertheless, astrometry from HST and Voyager is consistent with uniform, near-circular motion if one allows for a one-sigma increase in Naiad's Voyager-derived mean motion[7]; see Extended Data Table 3. The large ephemeris error implies that reported detections of Naiad from the W. M. Keck Telescope in 2002[8] were misidentifications. A 19° error in the predicted orbit of Thalassa[6] suggests that it may also have been misidentified in the same data set.

Determining the orbits of Hippocamp and Naiad entailed solving simultaneously for the orbits of all Neptune's inner moons. Table 1 lists our derived orbital elements: n = mean motion; a = semimajor axis; e = eccentricity; i = inclination; λ_0 = mean longitude at epoch; ϖ_0 = longitude of pericenter at epoch; Ω_0 = longitude of ascending node at epoch; ϖ' = apsidal precession rate; Ω' = nodal regression rate. Each orbit is defined relative to its local Laplace plane; this plane nearly aligns with Neptune's equator for the innermost moons, but

tilts toward the plane of Triton's orbit for larger *a*. The calculated angle of this tilt, ψ, is listed in Table 1. All of the Laplace planes share a common ascending node, which coincides with the descending node of Triton's orbit. We have determined orbits from HST data 2004–2016 only; for moons other than Hippocamp, more precise orbits could be obtained by also including prior detections from Voyager- and Earth-based telescopes[9]. Nevertheless, our orbital elements for the larger moons are in extremely close agreement with prior determinations[5–7].

Table 1 also lists the disk-integrated reflectivity D of each moon as obtained through broad visual filters. Our results generally agree with earlier Voyager photometry[10,11]. Extended Data Fig. 2 shows the moons' phase curves as needed to extrapolate the photometry to zero phase; see the Methods section for details. The other inner moons all have geometric albedos $k = 0.09 \pm 0.01$[11], so if Hippocamp is similar, its radius $R = 17.4 \pm 2.0$ km.

We can extrapolate the orbit of Hippocamp back to the time of the Voyager 2 flyby (August 25, 1989) with a precision of ± 0.5° in orbital longitude or ~ 10 pixels in Voyager's narrow-angle camera. Extended Data Table 4 lists the most sensitive candidate images that pointed at or near the predicted location. Any prediction that fell within 200 pixels of the field of view is listed. This same procedure accurately predicted all the best images of Neptune's other inner moons. All candidate images are either badly smeared or definitively missed Hippocamp based on its predicted position relative to the observed locations of other moons.

The Voyager images established an upper limit of ~ 5 km on the radius of any undiscovered moons[1] (assuming $k = 0.09$). That search was complete interior to $r = 65{,}000$ km and partially complete inside 90,000 km. Between the limits of the Voyager search and the orbit of Proteus, we can now rule out any moons half as bright as Hippocamp, implying $R \approx 12$ km. Beyond Proteus, our images are freer from Neptune's glare and orbital motion is slower, making it possible to coadd larger sets of images (Extended Data Fig. 3). Implant tests within these images indicate that a moon ~ 30% as bright as Hippocamp ($R \approx 10$ km) would generally be visible beyond Proteus. Our orbital coverage is complete out to $r \approx 200{,}000$ km and about 2/3 complete out to $r \approx 300{,}000$ km. However, moons on modestly inclined or eccentric orbits would be much harder to detect.

Using the orbital elements of Table 1 and methods previously applied to the Pluto system[12], we conducted an exhaustive search for resonances between these moons. No plausible Lindblad, corotation, or three-body resonances up to second order in (e, i) were found. The search was complete for numeric coefficients up to 200.

The discovery of tiny Hippocamp contributes to our understanding of the history of Neptune's inner system. Extended Data Figure 4 shows Hippocamp in context. It orbits just 12,000 km interior to Proteus, a body with 4,000 times its volume. Proteus and Hippocamp were even closer in the past, because Proteus is migrating outward due to tidal interactions with Neptune. Hippocamp, with its much lower mass, migrates very slowly and remains close to its point of origin. It is therefore worth exploring the possible connection between these moons.

Cometary impacts are thought to have disrupted Neptune's smallest moons multiple times; only Proteus is likely to have survived intact since shortly after the capture of Triton[1–3]. Pharos crater on Proteus is unusually large relative to the moon's size[13], suggesting that Proteus too may have come close to disruption. We hypothesize that a large impact, perhaps the Pharos event itself, released debris from Proteus into orbit around Neptune. Some of this debris settled into a stable orbit perhaps 1,000–2,000 km (a few Hill radii) interior to Proteus[14], and accreted into Hippocamp. Notably, the volume of Hippocamp is only ~ 2% of the missing volume associated with the Pharos impact basin[13]—literally, a rounding error.

This scenario has several complications. First, Proteus would probably have pumped up Hippocamp's e and i when the orbits were still very close, or perhaps later as it crossed a strong Hippocamp resonance[15]. It might therefore be surprising that e and i are very small, statistically indistinguishable from zero (Table 1). A later orbital disruption may provide a natural explanation; every time a moon is broken apart and re-accretes, its e and i are likely to be substantially reduced. The current formation rate for craters > 10 km on Proteus is ~ 10^{-12} km^{-2} y^{-1} [2]; the rate for Hippocamp should be similar. Hippocamp would be disrupted by any 10-km cratering event, so we infer that it has re-accreted ~ 9 times in the last 4 Gy.

For this scenario to work, Proteus must have migrated $\gtrsim$ 11,000 km in its lifetime. The migration rate is inversely proportional to Neptune's "quality factor" Q. For Proteus to migrate this distance in 4 Gy, Neptune's $Q \lesssim 15{,}000$[15]. This is compatible with the inferred range of Q for Neptune (12,000–330,000)[3] and also for Uranus (11,000–39,000)[16]. A smaller Q would imply that Proteus migrated further and therefore Hippocamp is somewhat younger. However, because the impactor flux was higher early in the solar system's history, Hippocamp is most likely at least a few Gy old.

However, one line of argument suggests an upper limit of 10,000 km on Proteus's migration. As Proteus crossed $r \approx 107{,}000$ km, it entered a 2:1 resonance with Despina, where simulations indicate that Despina's i should have grown to a value much larger than is currently observed[15]. However, because Despina is thought to have been disrupted 3–6 times in the last 4 Gy[2], this particular constraint on the migration of Proteus may not apply.

We cannot rule out the possibility that Hippocamp formed in situ and has no connection to Proteus. However, its tiny size and peculiar location lead us to favor this formation scenario, which illustrates the roles that collisions and orbital migration have played in shaping the Neptune system we see today.

METHODS

Data Selection:

Our data set encompasses most of HST's images of the Neptune system from 2004–2016. Only our own observing programs (GO-10398, 11656, and 14217) were capable of detecting Hippocamp, Naiad, and Thalassa, but the others provided detections of the larger moons, which contributed to the precision of our orbit solutions and photometry. Three programs that focused exclusively on imaging the planet through narrowband filters (GO-10423,

14044, and 14334) were omitted because of low sensitivity to the small satellites. We performed most of our analysis using calibrated ("FLT") image files. For the three smallest satellites, we used alternative calibrated images ("FLC") where available; these account for the charge transfer efficiency of the CCD and are expected to be more accurate for very faint targets. However, for our purposes, the difference was negligible.

Observing Techniques:

For our own observing programs, we employed broad visual-band filters, primarily CLEAR in ACS/HRC and F606W and F350LP in WFC3/UVIS. Neptune is typically observable for ~ 50 minutes of HST's orbit around the Earth, sufficient to obtain 8–11 very long exposures (175–320 s). Most visits also included a few short exposures for geometric and photometric reference.

All images were targeted at the center of Neptune. On some occasions, we performed dithering steps part way through an orbit of HST in order to prevent hot pixels from remaining at fixed locations. However, this was not strictly necessary; the moons move by many pixels within a single HST orbit, so no moon is ever affected by a hot pixel more than once. In 2016 (program GO-14217), we scheduled most of our visits to be split across two orbits to improve coverage in orbital longitude; each half-orbit contained 5 or 6 long exposures.

Most observations were scheduled to keep Triton outside the field of view. However, this was not always possible and observations of Triton contributed to our analysis, in particular because the orbit of Triton defines the orientation of the Laplace planes.

During 2004 (program GO-10398; see Fig. 1a), we used the occulting mask on the HRC to suppress excess light from Neptune. Although the mask was designed to obscure point targets, we found it to be quite successful at suppressing the glare from Neptune. The 3″ mask only barely covered Neptune's 2.4″ disk, requiring us to center Neptune with fine precision. The process of positioning the coronagraph is automated; the camera takes an image and then shifts the pointing to place the brightest pixel at the center of the mask. We found that Neptune is a featureless disk in ultraviolet light and so we used filter F330W (with passband 0.33 ± 0.03 μm) for the initial pointing. This procedure worked every time.

We also developed other techniques to suppress the light from Neptune in the absence of a coronagraph. The CCDs on HST "bloom" along the *y*-axis when saturation occurs, but this generally does not corrupt pixels that are offset along the *x*-axis. During 2005 (Fig. 1b) we simply shortened our exposure times to limit the distance over which the bloom would occur. In 2009 and 2016 (Figs. 1c,d) we chose observing periods around opposition, when we could orient the camera with the rings and satellites along the *x*-axis. In these cases, overexposing Neptune is essentially harmless.

Image Processing:

Although we were able to control Neptune's saturation using methods described above, glare from Neptune was ever-present and, as with all long exposures on HST, cosmic rays created a smattering of "snow" atop most images (Extended Data Fig. 5a). Hot pixels fall at

known locations in each image and are cataloged for each detector. Cosmic ray hits were recognized as clusters of pixels in one image that differ by more than three standard deviations from the median of identical exposures from the same HST orbit. For cosmetic purposes, we overwrote these pixels with the median of the adjacent pixels (Extended Data Fig. 5b). However, we also kept track of overwritten pixels using a boolean mask and ensured that masked pixels were ignored in the subsequent data analysis (Extended Data Fig. 5c). We suppressed the glare and diffraction spikes by aligning the center of Neptune in all the images from each HST visit that shared a common filter. We constructed a background image from the median value among all the pixels after aligning on the center of Neptune. Unlike the mean, the median is not affected by moons (which move rapidly) or cosmic ray hits (which are transient). The resulting images were therefore a smooth representation of Neptune's glare and diffraction spikes. Subtracting the backgrounds yielded individual images that were almost free of distracting gradients (Extended Data Fig. 5d).

Our specific processing steps were always adapted to the scientific goals. For astrometry of all but the smallest three moons, we worked with unprocessed images because we did not want to corrupt the PSF and because we could handle the glare as part of our modeling. For Naiad, Thalassa, and Hippocamp, all of the above steps were required because the most important consideration was to maximize visual detectability (Figs. 1 and 2; see Extended Data Tables 1,2).

Small Moon Detections:

The three smallest moons, Naiad, Thalassa and Hippocamp, required additional effort to detect. We performed a procedure akin to "unsharp mask", in which we subtracted the median of the nearby pixels (in a box ranging in size from a 7×7 to 13×13, depending on the circumstances) from each pixel in a given image. Normally, unsharp masking uses the mean, not the median, but the median suppresses most of the artifacts produced by the mean, such as creating dark circles around bright features. This step removed the last remaining background gradients from the images (Extended Data Fig. 5e).

We customized the image distortion and coadding procedure for each moon, based on the number of images required to obtain a usable detection. Hippocamp almost always required the coadding of an entire HST orbit (8–11 images). Naiad could often be detected in half-orbits of coadded data; this allowed us to obtain two measurements per HST orbit rather than one. Thalassa could sometimes be seen in individual images, but in other cases it was necessary to coadd two or more. We described our coadding procedure above (Fig. 2). Once we detected a body, we adopted a slightly different image processing procedure to optimize the images for our analysis. That was to transform each set of images using the fixed mean motion n_{m} for each moon as determined during the discovery/recovery process:

$$\mathbf{x}_1 = \mathbf{x}\left(r\left(\mathbf{x}_0\right), \theta\left(\mathbf{x}_0\right) + n_{\mathrm{m}} \times \left[t_1 - t_0\right]\right) \quad [2]$$

This transform is preferred because it does not create a spiral pattern that arises when n is treated as a function of r, so it is less disruptive to the PSFs.

When searching for moons outside the orbit of Proteus (Extended Data Fig. 3), motion is slow enough that we could coadd images spanning a few adjacent orbits. In these cases, we transformed the images using polar coordinates, so that the longitude at epoch varies from 0 to 360° along the *x*-axis and radius increases along the *y*-axis:

$$x = \theta(\mathbf{x}_0) + n(r(\mathbf{x}_0)) \times [t_1 - t_0] \quad [3a]$$

$$y = r(\mathbf{x}_0) \quad [3b]$$

Astrometry:

Because Neptune is large and often saturated, is was unusable as a pointing reference. Background stars could have also provided pointing references but these are generally absent. As a result, we performed an initial navigation (pointing correction) for each image by searching for the brightest moons by eye. We could easily obtain initial precision of 1–2 pixels, at which point it became practical to search for the known moons using an automated procedure. However, all detections were inspected visually and rejected if the moon could not be clearly seen or if something nearby might have corrupted the measurement. Naiad, Thalassa, and Hippocamp were too small to be detected in this way and were handled by an entirely manual process, as discussed further below.

For each measurement, we fitted a model PSF to a small square of the image surrounding each detectable body. Model PSFs were generated using the "Tiny Tim" software maintained by STScI[17]. The parameters to be fitted included the center position (*x, y*), the scaling factor to match the brightness of the body, and parameters to define an underlying 2-D ramp of background light. The background ramp was needed to account for Neptune's glare. Nearest the planet, we used a 2-D quadratic requiring six additional free parameters; elsewhere, we used a 2-D linear function requiring just three.

For the faintest moons, we adopted a slightly different procedure. Many of these images had been distorted and coadded, so the PSF was no longer accurately described by the Tiny Tim model. Instead we used a uniform 2-D gaussian for the PSF. Given how faint these objects are in our data, this simpler PSF model was adequate for our needs. To handle the possibility of a bias between the center of the model PSF and the gaussian, we performed the same gaussian fits on Despina, Galatea, and Larissa, and then calculated the mean offset between the PSF's center and the gaussian's center. We applied these corrections, typically a few hundredths of a pixel, to the center location of each gaussian fit.

We solved for the best-fit values of (*x,y*) via straightforward nonlinear least-squares fitting (Extended Data Tables 1–2; Table 1 source data). We estimated the uncertainties by linearizing the model around the best-fit solution and then solving for the covariance matrix. This procedure generally provided a reliable estimate of the uncertainties—typically, a few tenths of a pixel. By chance, however, some error bar estimates were clearly too small; this created difficulties when fitting orbits because the measurements, although extremely

accurate, produced anomalously large residuals in units of the standard deviation σ. We solved this problem by setting 0.1 pixels as the absolute floor for σ.

Orbit Models:

We describe the orbit of each moon using nine orbital elements (Table 1). However, we reduce the number of free parameters to six by using Neptune's known gravity field to derive the values of semimajor axis (a), apsidal precession rate (ϖ'), and nodal regression rate (Ω') from the mean motion n, eccentricity e, and inclination i. The relationship we used is accurate to second order in (e, i)[18]. We used GM = 6835099.5 km^3/s^2; $J_2 = 3408.43\times10^{-6}$; $J_4 = -33.40\times10^{-6}$, assuming Neptune's radius is 25,225 km[6]. Our reference epoch is midnight 2009 January 1 UTC, chosen because it falls near the mid-time of all our observations. In Barycentric Dynamical Time (TDB), this is 284,040,066.184 seconds after the J2000 epoch (2000 January 1.5 TDB).

Triton's orbital inclination is 157.4°, meaning that it is both retrograde and tilted away from Neptune's equator by 22.6°. Its nodal regression period is ~ 600 years. Over that interval, the pole of Triton's orbit sweeps out a cone of half-width 22.2° while Neptune's rotation pole sweeps out a cone of 0.5°. This polar wander is rapid enough that it must be accounted for when describing the orbits of the inner moons. Furthermore, Triton tilts the Laplace planes of the moons away from Neptune's equator and toward its own orbital plane. We follow methods described elsewhere[7] to determine the tilt of each moon's Laplace plane (Table 1).

Note that, for Triton's orbit, we described the shape and orientation using prograde angles, but reversed the signs of n, ϖ', and Ω'. Furthermore, we held n, a, and Ω' fixed in our analysis but used our own astrometry to define the remaining elements. We chose this approach because (a) our time baseline for Triton was quite short compared to that of previous studies[6], (b) these quantities define the orientation of the Laplace plane, which affects all the remaining moons, but (c) vagaries in the definition of the longitude reference (discussed below) left us uncomfortable depending entirely on the published orbital elements. However, our results were quite compatible with previous results; see Extended Data Table 3.

Defining an appropriate reference longitude in the context of misaligned planes and precessing poles is challenging. Ideally, we seek an inertially fixed definition that is independent of epoch. Notably, previous papers on the orbits of Neptune's inner moons have adopted many different references, none of which meet these requirements. The common node of all the Laplace planes is a tempting reference point, but it is not well determined and, of course, it rotates every 600 years. For this investigation, all longitudes were measured from the ascending node of the Neptune system's invariable plane on the ICRF (International Celestial Reference Frame) equator. This is a fixed direction in space. The pole of this plane has right ascension 299.46 ± 0.14° and declination 43.40° ± 0.03°[5]. The uncertainties are small; any future change in the best-fit invariable pole will merely introduce a small, constant offset to the orbital elements λ_0, ϖ_0, and Ω_0. From this reference direction, all longitudes are measured as broken angles along the invariable plane to the common ascending node of all the Laplace planes, thence along each moon's Laplace plane to its orbital ascending node, and thence along the orbit plane. Using this frame definition,

we can update all published orbital elements to a common epoch (Extended Data Table 3). All orbits are in good agreement for Despina, Galatea, Larissa, and Proteus. Naiad's orbit agrees with the Voyager-era solution[7] if one increases its mean motion by 1σ; the 2004 solution[6] disagrees with this work because it includes an erroneous measurement. We also note that the orbit solutions for Thalassa appear to be diverging, although all solutions agree at the Voyager epoch.

Orbit Fitting:

We converted our astrometry from (*x,y*) coordinates to right ascension and declination using the published distortion models for the HST cameras[19]. In the case of images taken using the unsupported CLEAR filter on ACS/HRC, later analysis showed persistent, large residuals. By experimentation, we determined that this was caused by a plate scale error; a scale correction factor of 0.9987 made the problem go away.

The fitting process requires a simultaneous solution for the orbital elements of every moon plus the precise navigation of every image. As in previous analyses of HST images[12,20], we have assumed that HST does a perfect job of tracking the position of Neptune within each HST orbit. Thus, one need not determine a unique pointing correction for every image; instead, images obtained through the same filter during a single orbit can reliably share a common navigation. Images taken through different filters are navigated independently, however, because the optical paths are different and shifts of up to 0.5 pixels were sometimes noted. The Table 1 source data lists, for every image, the reference image to which its navigation was tied.

Our initial analysis focused on the five best-observed moons: Despina, Galatea, Larissa, Proteus, and Triton. Because the parameters describing image navigations and those describing the orbits are only weakly coupled, it was practical to fit the orbits and navigate the images via iteration. First, we would solve for the orbital elements of all five moons while holding the navigations fixed. Second, we held the orbits fixed and solved for improved navigations. Repeating the process quickly led to convergence for both sets of parameters. Most navigations were quite precise; the median uncertainty was 0.01 pixel and the mean was 0.05. At each iteration, we used the best-fit determination of Triton's descending node to define the Laplace planes for the other moons. After this process completed, we held the navigations fixed while solving for the orbits of the smaller moons.

Not unexpectedly, this analysis revealed that a small number of our measurements were erroneous. This is related to the fact that the astrometric errors do not obey a normal distribution; the distribution has an extended tail due to the small but nonzero possibility that the fitting procedure will converge on the wrong point. Investigating the distribution revealed that the break between the gaussian behavior and the extended tail occurred near 3σ. We therefore categorized each measurement with residuals below 3σ as valid and those with residuals ≥ 5σ as clearly invalid. Invalid measurements were rejected outright, whereas measurements between 3σ and 5σ were regarded as probably erroneous. Including them in the fit could bias our answers, but excluding them would artificially reduce our assessment of the uncertainties. Our solution was to exclude them from the fit, but then to apply an enhancement factor to the overall goodness of fit (GOF = χ^2 per degree of freedom)

following a procedure to compensate for the possible bias. This method involves a "Monte Carlo" simulation of what the enhancement factor would need to be if the astrometry were truly gaussian-distributed and we omitted the 3σ outliers; details are discussed elsewhere[12].

Photometry:

We obtained photometry from images taken through the filters CLEAR, F606W, and F350LP, all having passbands comparable to a very wide V filter. We measured Despina, Galatea, Larissa, and Proteus's "ensquared energy" by summing the pixel values inside square boxes centered on the known location of each moon. Each sum was corrected for an estimate of the mean local background by averaging the pixels in a surrounding border 1–3 pixels wide. Each of these measurements undercounts the photons from a point source, however, because the PSFs have extended tails. We determined the correction factor for each box size based on tabulations of the ensquared energy correction factor for UVIS[21], and adapted a table of encircled energy for HRC[22].

The optimal box size for a given moon depends on circumstances: smaller boxes provide less precision because of small number statistics and the large correction factor, whereas large boxes are more likely to be corrupted by background variations and/or bad pixels. To handle this in an automated manner, we calculated the sums for each moon in each image using up to 18 combinations of box size and border width. Each measurement was corrected for the PSF as described above, and then we derived a robust mean using the "biweight" algorithm[23]. Afterward, we derived the robust mean and standard deviation among all the measurements of each moon as observed through the same filter during the same HST orbit.

For Naiad, Thalassa, and Hippocamp, we were using coadded images with distorted PSFs, so the above procedure was inappropriate. Instead, we obtained results simultaneously with our astrometry by recording the volume under the fitted gaussian. To correct for the undercount, we performed the same analysis on the four larger moons and used that to derive a correction factor for each instrument, filter, and box size. We then applied this factor, which was typically in the range 2–3, to each measurement.

We converted from raw image values to the calibrated, disk-integrated reflectivity D as follows. The file header of every calibrated Hubble data product contains a parameter value PHOTFLAM, the image's "inverse sensitivity" in units of erg/cm^2/Å/s. PHOTFLAM, multiplied by the exposure time, converts the numbers in the image array to intensity I in physical units of erg/cm^2/Å. Reflectivity is the dimensionless ratio of I to F, where πF is the incoming solar flux density. We calculate F by averaging the solar spectrum (as defined by STScI data product "sun_reference_stis_001.fits") over the throughput of each instrument and filter. The resulting value is as would be measured at one astronomical unit (AU), so we divided F by the square of the Sun-Neptune separation distance in AU for the time of each visit. The resulting factor would be appropriate to determine the reflectivity of an extended source. For an unresolved point source, we also multiply by the projected area of a pixel in units of km^2. The resulting quantity, when multiplied by the sum of the pixel values within the PSF of a point source, is D. Individual values are listed in the source data for Table 1.

We normalized all measurements to compensate for the irregular shapes of the moons, modeling them as triaxial ellipsoids using published values for the three radii (a,b,c)[11]. Due to tidal locking, the long axis (a) points toward Neptune and the short axis (c) is normal to the orbit plane. The projected cross-section A of a moon depends on the sub-Earth longitude Θ (measured from the long axis) and latitude Φ as follows:

$$A = \pi\left[(bc\cos\Theta\cos\Phi)^2 + (ac\sin\Theta\cos\Phi)^2 + (ab\sin\Phi)^2\right]^{1/2}. \quad [4]$$

Using this formula, we re-scaled all measurements to (Θ,Φ) (90°,−27°), because our best photometry was obtained near this geometry. Shape corrections were typically less than 5%.

Extended Data Fig. 2 shows the phase curves for all of the inner moons. Measurements span phase angles α = 0.03–1.92°. The moons all show a marked opposition effect, typically with a slope of 0.2 magnitudes per degree. Note that this surge is much steeper than the phase function slope measured from Voyager images at $\alpha > 12°$[10,11]. The moons' phase curves and color properties warrant further study but that topic is beyond the scope of this paper.

Because we have many measurements where $\alpha < 0.1$, a linear fit to the data provided an accurate measure of each moon's visual, disk-integrated photometry at zero phase. These are the values identified as D in Table 1. The effective radius R is $[D/(\pi k)]^{1/2}$, where $k = 0.09 \pm 0.01$[11].

Data Availability:

All source data used in this study is in the public domain and may be requested from the STScI archive at http://archive.stsci.edu/hst/search.php. The Voyager images referenced in this paper can be retrieved from NASA's Planetary Data System at https://pds-rings.seti.org/viewmaster/volumes/VGISS_8xxx/VGISS_8207. Data files representing every image analyzed for this investigation at nearly every intermediate step in its analysis are permanently archived at http://dmp.seti.org/mshowalter/neptune_xiv.

Code Availability:

Python 2.7 source code that implements all the key image processing steps is permanently archived at http://dmp.seti.org/mshowalter/neptune_xiv/software. Orbit fitting and image geometry calculations are widely used procedures for which many implementations exist; we have documented all our procedures in detail but have not distributed our own custom source code.

Extended Data

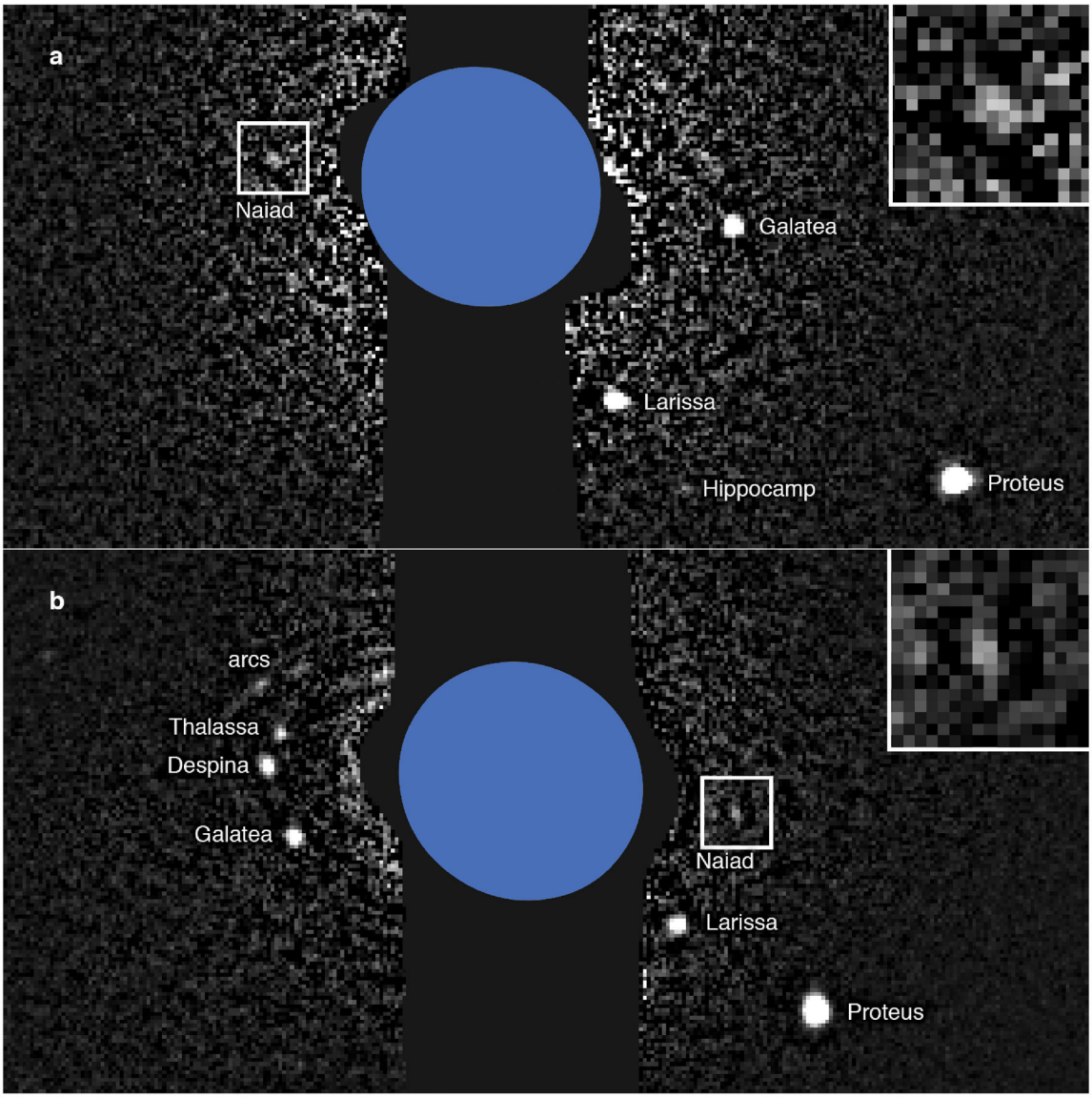

Extended Data Fig. 1 |. Recovery of Naiad

Each panel shows a portion of an HST image after processing and coadding as described in the text. The location of Naiad in each panel is indicated by a small square; a closeup is inset at upper right. The outline of Neptune's disk is indicated by a blue ellipse. **a**, View from Visit 01, orbit 1 of HST program GO-11656, obtained on 2009 August 19. It shows the first unambiguous detection of Naiad since the 1989 Voyager flyby of Neptune. **b**, View from Visit 08, orbit 2 of program GO-14217, taken on 2016 September 2.

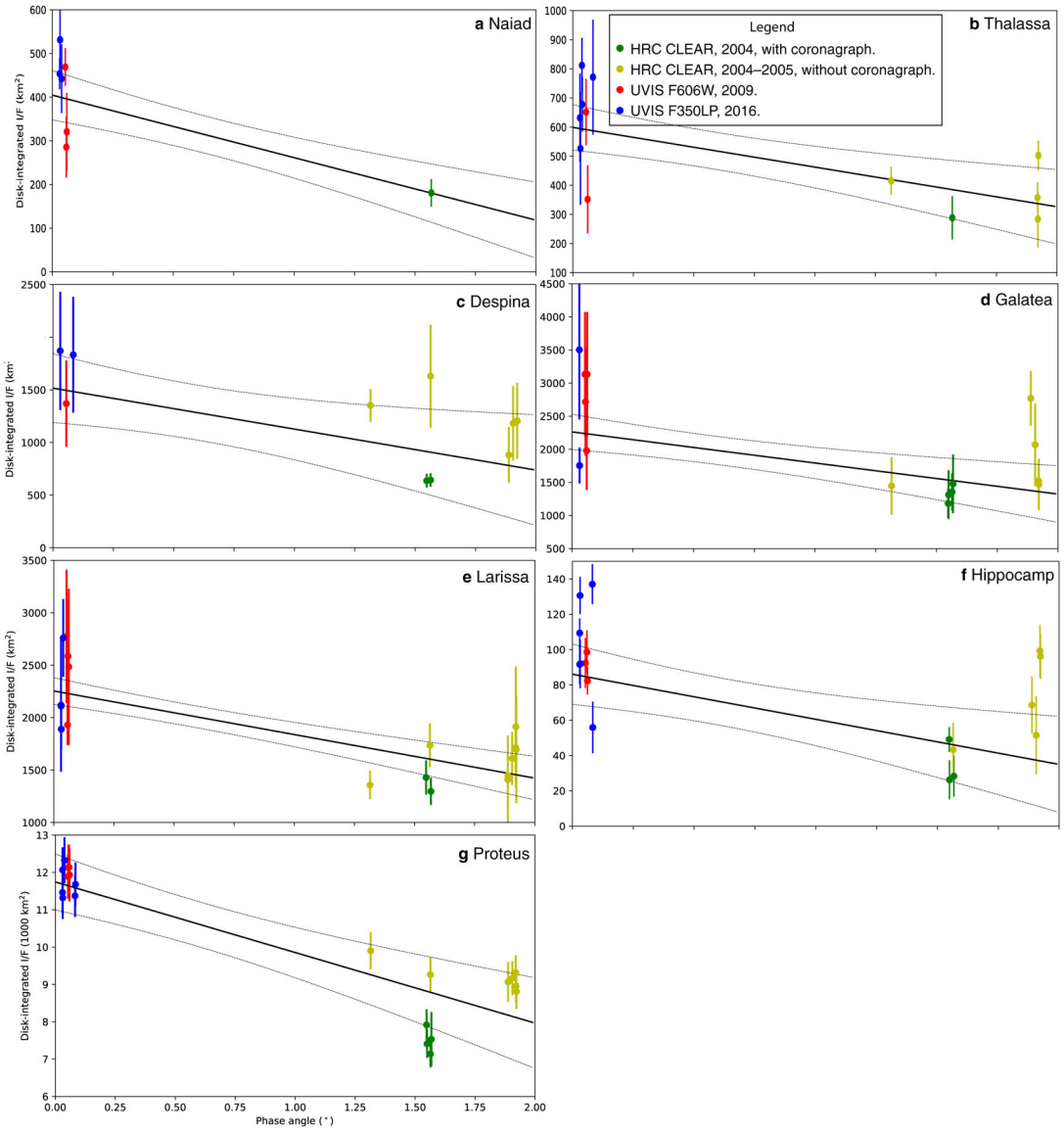

Extended Data Fig. 2 |. Phase curves of Neptune's inner moons

Each panel shows measurements of disk-integrated reflectance D vs. phase angle for one of Neptune's inner moons through broad, visual filters. Error bars are ± 1σ. Colors indicate the instrument, filter and observing mode as defined in the legend. Solid lines are a least-squares linear fit to the data; dotted lines indicate the range of the uncertainty in the model, ± 1σ, as derived from the covariance matrix of each fit. The values in Table 1 correspond to the mean and uncertainty extrapolated to $\alpha = 0$.

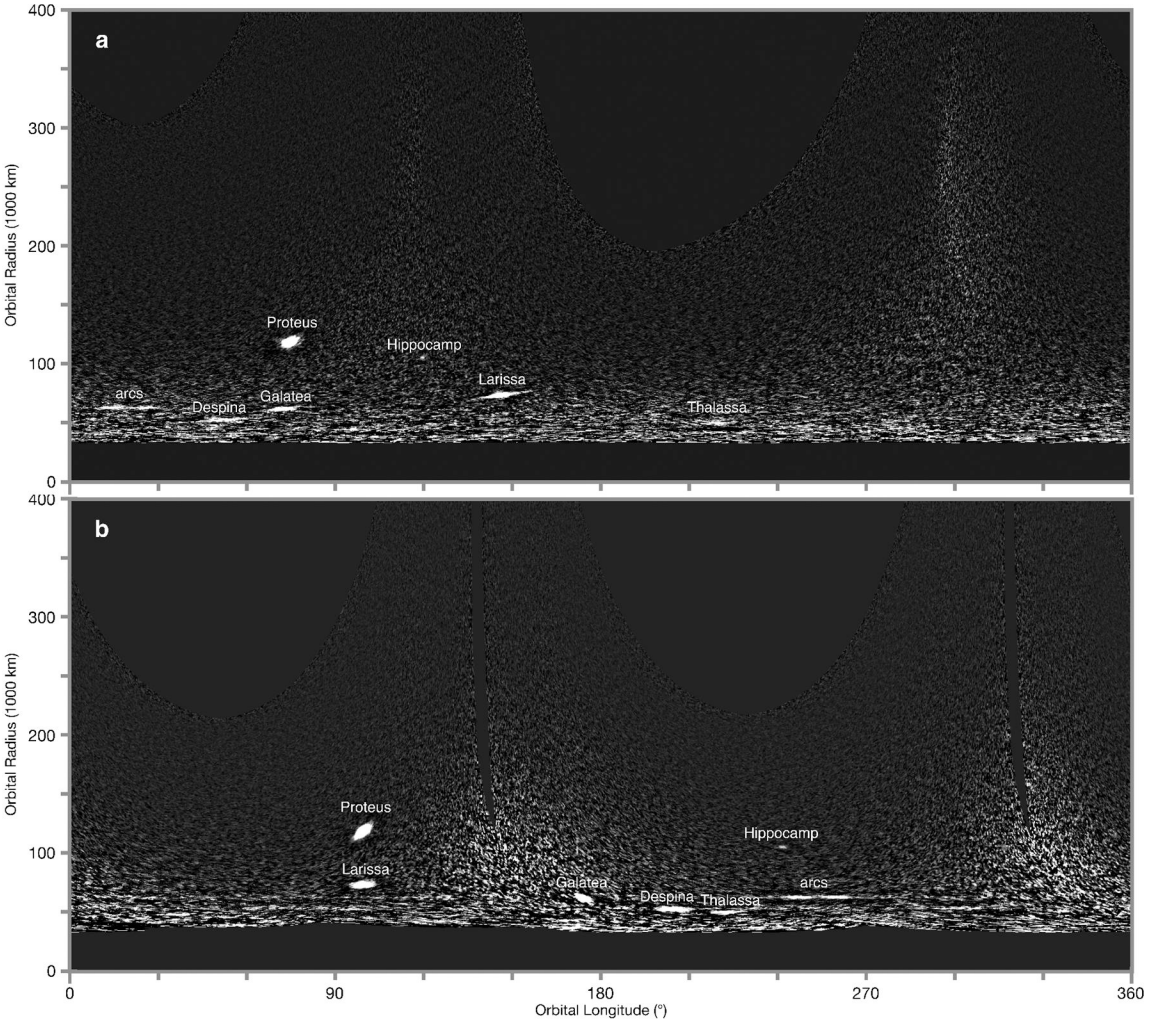

Extended Data Fig. 3 |. Deep searches for small moons

Each panel shows multiple HST images coadded into a “map” in which longitude increases from 0 to 360° along the horizontal axis and radial position is 0 to 400,000 km along the vertical axis. **a**, View derived from the five HST orbits of program GO-11656, obtained on 2009 August 19. **b**, View from the two orbits of Visit 03 in HST program GO-14217, taken on 2016 September 2.

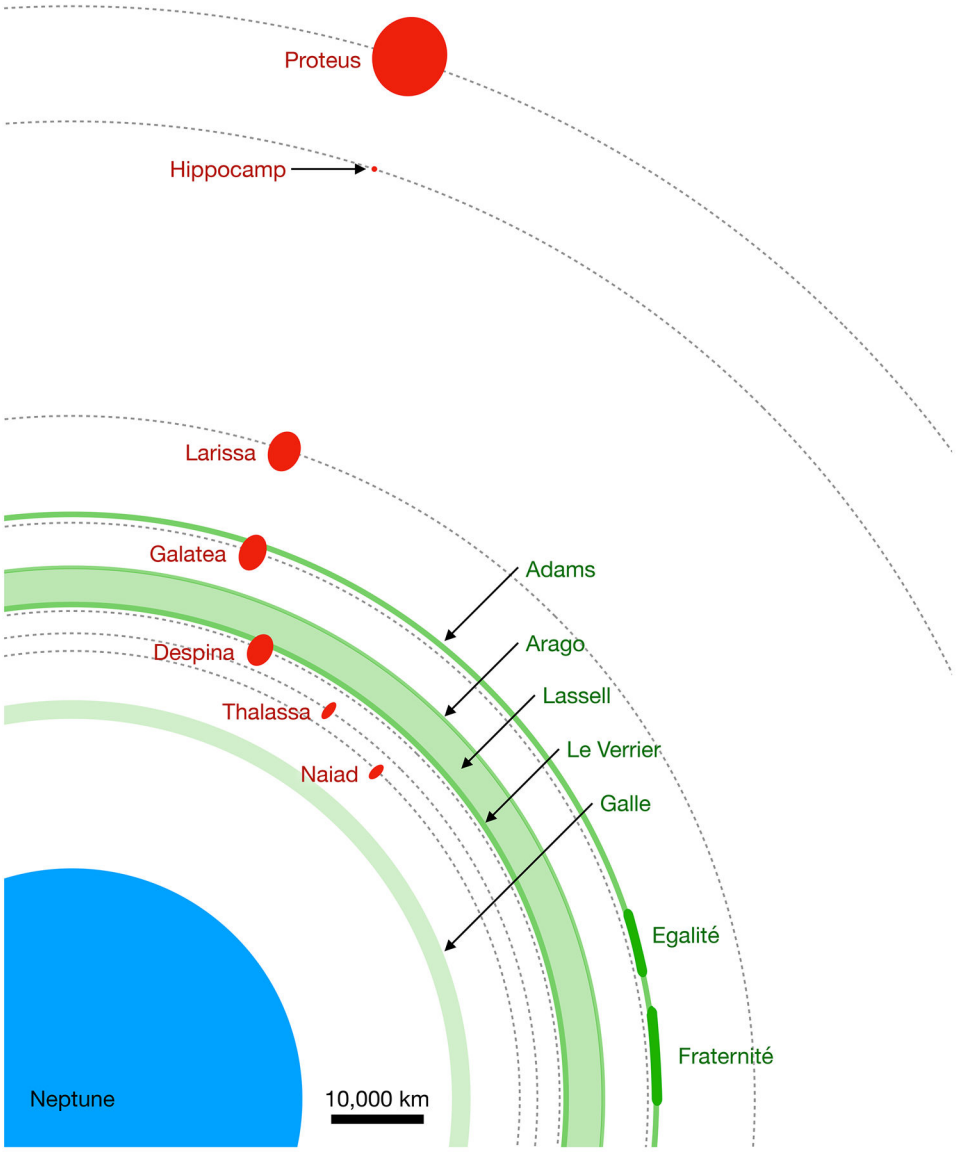

Extended Data Fig. 4 |. Diagram of the Neptune system

All of the known features of the Neptune system interior to Triton are shown to scale. (Triton orbits about three times further out than Proteus.) Rings and arcs are shown in green. Moon shapes are indicated by red ellipses indicating their dimensions $a \times c$, enlarged relative to their orbits by a factor of 20.

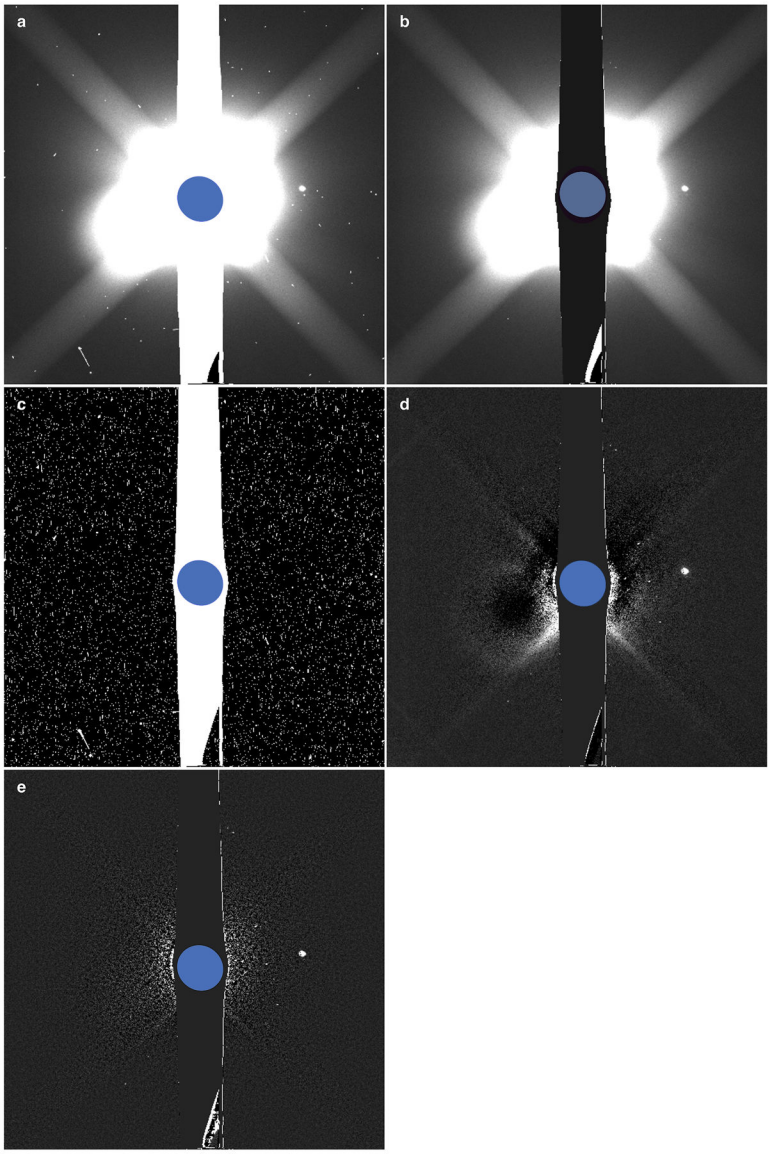

Extended Data Fig. 5 |. Image processing steps illustrated

a, Image icwp01n7q_flt.fits taken on 2016 August 31. **b**, The image after hot pixels and cosmic ray hits have been removed. **c**, The boolean mask where white indicates pixels that will be ignored from further analysis. **d**, The image after the mean of other images from the same HST visit have been averaged and subtracted. This step removes most of the glare. **e**, The image after an “unsharp mask” process involving the subtraction of a median-filtered version of the same image. The outline of Neptune’s disk is indicated by a blue ellipse in each panel.

Extended Data Table 1 |

Measurements of Hippocamp obtained for this study

Target Image	Coadded Images	Integration (min)	Filter	Exposure Midtime		*X*	*Y*	ΔRA (arcsec)	Δdec (arcsec)	*D* (km^2)	SNR
j95m01evq_flt_h.fits	3	5.8	CLEAR	2004-11-06T10:26:48		419.847	983.368	−4.71005	−0.52841	68.6	4.3
	eu;ev;f1				±	0.153	0.236	0.00544	0.00544	16.1	
j95m03ifq_flt_h.fits	8	29.6	CLEAR	2004-12-08T07:18:46		442.524	606.458	4.61184	1.11939	28.3	2.4
	ib-ii				±	0.096	0.110	0.00287	0.00287	11.6	
j95m04o7q_flt_h.fits	8	29.6	CLEAR	2004-12-09T07:18:56		415.280	613.995	4.18700	1.76485	26.2	2.4
	o3-oa				±	0.137	0.132	0.00377	0.00377	11.0	
j95m04ogq_flt_h.fits	10	37.0	CLEAR	2004-12-09T08:41:53		389.243	652.976	3.14392	2.27683	49.1	7.0
	ob-ol				±	0.166	0.115	0.00407	0.00407	7.0	
j95m06c7q_flt_h.fits	10	7.5	CLEAR	2005-04-01T20:14:51		476.950	366.555	−4.18766	−1.90511	43.3	2.8
	by-cg				±	0.193	0.187	0.00531	0.00531	15.2	
j95m07zaq_flt_h.fits	10	7.5	CLEAR	2005-05-06T23:01:47		529.614	331.725	−4.59666	−1.49335	96.2	7.5
	z1-zj				±	0.266	0.206	0.00673	0.00673	12.8	
j95m08s6q_flt_h.fits	10	7.5	CLEAR	2005-05-12T05:21:29		537.735	721.063	4.23993	2.00512	99.2	6.7
	rx-sf				±	0.207	0.204	0.00577	0.00577	14.8	
j95m10dwq_flt_h.fits	10	7.5	CLEAR	2005-05-17T00:28:38		559.740	694.139	3.45392	2.41691	51.5	2.3
	dn-e5				±	0.201	0.204	0.00567	0.00567	22.1	
ib2e01vyq_flc_h.fits	8	36.7	F606W	2009-08-19T09:49:25		225.504	204.913	1.94315	2.89369	92.4	6.5
	vu-w1				±	0.299	0.200	0.01042	0.01042	14.2	
ib2e02z5q_flc_h.fits	8	36.7	F606W	2009-08-19T14:37:13		159.100	213.065	−3.66390	0.42630	98.6	8.0
	z1–z8				±	0.304	0.302	0.01241	0.01241	12.3	
ib2e02zmq_flc_h.fits	8	36.7	F606W	2009-08-19T16:08:47		122.376	220.431	−4.54516	−0.79672	82.3	10.6
	zi-zp				±	0.099	0.095	0.00400	0.00400	7.8	
icwp01n4q_flc_h.fits	5	14.6	F350LP	2016-08-31T08:29:35		375.159	273.003	4.33084	2.25431	55.9	3.8
	n2–n6				±	0.198	0.198	0.00812	0.00812	14.6	
icwp01n9q_flc_h.fits	6	17.5	F350LP	2016-08-31T09:54:26		386.764	257.339	3.94639	3.01685	137.0	12.1
	n7-nc				±	0.107	0.105	0.00435	0.00435	11.3	
icwp02blq_flc_h.fits	5	14.6	F350LP	2016-09-02T08:11:09		370.531	210.993	3.53758	3.22970	91.9	6.7
	bj-bn				±	0.095	0.109	0.00419	0.00419	13.8	
icwp02bqq_flc_h.fits	6	17.5	F350LP	2016-09-02T09:35:53		348.195	203.966	2.32684	3.28363	130.6	12.4
	bo-bt				±	0.180	0.181	0.00740	0.00740	10.5	
icwp03d4q_flc_h.fits	5	14.6	F350LP	2016-09-02T17:37:15		130.693	259.309	−4.33879	−2.33913	91.6	8.0
	d2–d6				±	0.182	0.172	0.00725	0.00725	11.5	
icwp03d9q_flc_h.fits	6	17.5	F350LP	2016-09-02T17:56:53		134.089	269.453	−4.29093	−2.54418		
	d7-dc				±	0.114	0.124	0.00488	0.00488		
icwp03djq_flc_h.fits	5	14.6	F350LP	2016-09-02T19:11:40		132.450	282.777	−3.79933	−3.11553	109.3	13.2
	dh-dl				±	0.121	0.120	0.00494	0.00494	8.3	
icwp03dqq_flc_h.fits	6	17.5	F350LP	2016-09-02T19:31:18		140.841	292.191	−3.59005	−3.20677		
	do-dt				±	0.108	0.102	0.00430	0.00430		

Target Image	Coadded Images	Integration (min)	Filter	Exposure Midtime		*X*	*Y*	ΔRA (arcsec)	Δdec (arcsec)	*D* (km^2)	SNR
icwp04ijq_flc_h.fits	5	14.6	F350LP	2016-09-03T09:37:18		320.212	207.023	0.99358	2.94761	225.0	11.2
	ih-il				±	0.314	0.308	0.01275	0.01275	20.1	

Target image defines the geometry of each measurement after the specified set have been distorted and coadded. Locations (*X*, *Y*) are in absolute pixel coordinates, where (0,0) refers to the center of the lower left pixel in the image. ΔRA and Δdec are measured offsets from the center of Neptune. Uncertainties (1σ) appear directly below each associated value. Uncertainties in RA and dec are treated as equal. SNR is the statistical significance of the detection. Where *D* is missing, multiple measurements from the same HST orbit have been merged into a single value shown above it.

Extended Data Table 2 |

Measurements of Naiad obtained for this study

Target Image	Coadded Images	Integration (min)	Filter	Exposure Midtime		*X*	*Y*	ΔRA (arcsec)	Δdec (arcsec)	*D* (km^2)	SNR
j95m03ifq_flt_n.fits	3	11.1	CLEAR	2004-12-08T07:18:46		447.764	882.189	−2.06041	−0.61781	181.2	5.7
	id-if				±	0.223	0.242	0.00651	0.00651	32.0	
ib2e01vvq_flc_n.fits	4	18.3	F606W	2009-08-19T09:33:10		123.819	282.561	−2.01216	−0.03538	365.9	10.8
	vu-vx				±	0.199	0.158	0.00736	0.00736	33.9	
ib2e01vzq_flc_n.fits	4	18.3	F606W	2009-08-19T09:54:50		118.458	292.112	−2.21316	−0.40442		
	vy-w1				±	0.276	0.266	0.01110	0.01110		
ib2e01ycq_flc_n.fits	4	18.3	F606W	2009-08-19T12:41:10		211.801	289.305	1.51768	−0.41238	256.5	4.1
	yb-ye				±	0.406	0.405	0.01660	0.01660	62.8	
ib2e01ygq_flc_n.fits	4	18.3	F606W	2009-08-19T13:02:50		223.523	278.360	1.97107	0.00364		
	yf-y1				±	0.263	0.257	0.01065	0.01065		
ib2e02z2q_flc_n.fits	4	18.3	F606W	2009-08-19T14:20:58		273.630	277.791	1.67518	1.11004	264.8	3.6
	z1–z4				±	0.438	0.438	0.01794	0.01794	73.2	
icwp02bkq_flc_n.fits	2	5.8	F350LP	2016-09-02T08:07:20		205.526	248.834	−1.93850	−0.45324	529.6	7.8
	bj-bk				±	0.469	0.459	0.01901	0.01901	67.9	
icwp02bmq_flc_n.fits	3	8.8	F350LP	2016-09-02T08:14:58		202.733	251.872	−1.99146	−0.60242		
	bl-bn				±	0.205	0.206	0.00842	0.00842		
icwp02bpq_flc_n.fits	3	8.8	F350LP	2016-09-02T09:32:04		215.269	287.926	−1.19946	−1.62137	568.8	7.2
	bo-bq				±	0.357	0.365	0.01479	0.01479	79.3	
icwp02bsq_flc_n.fits	3	8.8	F350LP	2016-09-02T09:43:31		222.884	289.936	−0.88472	−1.58766		
	br-bt				±	0.301	0.275	0.01181	0.01181		
icwp03diq_flc_n.fits	2	5.8	F350LP	2016-09-02T19:07:51		312.340	257.061	2.03039	0.96539	449.3	12.8
	dh-di				±	0.307	0.280	0.01204	0.01204	35.1	
icwp03dkq_flc_n.fits	3	8.8	F350LP	2016-09-02T19:15:29		312.982	253.043	1.97173	1.11473		
	dj-dl				±	0.300	0.301	0.01232	0.01232		
icwp03dpq_flc_n.fits	3	8.8	F350LP	2016-09-02T19:27:29		318.702	252.912	1.89372	1.30350		
	do-dq				±	0.181	0.164	0.00708	0.00708		
icwp03dsq_flc_n.fits	3	8.8	F350LP	2016-09-02T19:38:56		317.252	248.502	1.75323	1.42909		
	dr-dt				±	0.290	0.279	0.01166	0.01166		
icwp04iiq_flc_n.fits	2	5.8	F350LP	2016-09-03T09:33:29		313.127	255.198	1.90079	1.25313	406.4	5.6
	ih-ii				±	0.161	0.157	0.00652	0.00652	72.6	
icwp04ikq_flc_n.fits	3	8.8	F350LP	2016-09-03T09:41:07		313.536	251.923	1.83671	1.36675		
	ij-il				±	0.159	0.162	0.00658	0.00658		

Target image defines the geometry of each measurement, after the specified set have been distorted and coadded. Locations (X, Y) are in absolute pixel coordinates, where (0,0) refers to the center of the lower left pixel in the image. ΔRA and Δdec are measured offsets from the center of Neptune. Uncertainties (1σ) appear directly below each associated value. Uncertainties in RA and dec are treated as equal. SNR is the statistical significance of the detection. Where D is missing, multiple measurements from the same HST orbit have been merged into a single value shown above it.

Extended Data Table 3 |

Comparison of projected mean longitudes at three epochs

				As Published		1989-08-18.5 TDB	2000-01-01.5 TDB	2009-01-01.0 UTC
Orbit & Referen	**Epoch**	**Origin (°)**		**λ (°)**	**n (°/day)**	**λ (°)**	**λ (°)**	**λ (°)**
Naiad								
O 1991 [6]	1989-08-18.5 TDB	0.202		60.260	1222.844100	60.463	73.913	54.829
			±	0.042	0.013800	0.042	52.274	97.642
JO 2004 [5]	1989-08-18.5 TDB	352.424		68.103	1222.843579	60.528	72.005	51.207
			±	0.035	0.000804	0.035	3.046	5.689
This work	2009-01-01.0 UTC			156.354	1222.858303	61.493	128.746	156.354
			±	0.248	0.000133	0.977	0.504	0.248
Thalassa								
O 1991 [6]	1989-08-18.5 TDB	0.202		239.737	1115.755600	239.939	322.152	329.542
			±	0.028	0.010100	0.028	38.259	71.463
JO 2004 [5]	1989-08-18.5 TDB	352.424		247.581	1155.755977	240.005	283.646	32.306
			±	0.025	0.000236	0.025	0.894	1.670
This work	2009-01-01.0 UTC			50.874	1155.758516	240.608	293.867	50.874
			±	0.077	0.000033	0.248	0.134	0.077
Despina								
O 1991 [6]	1989-08-18.5 TDB	0.202		85.272	1075.734200	85.474	126.623	323.630
			±	0.014	0.002800	0.014	10.606	19.811
JO 2004 [5]	1989-08-18.5 TDB	352.424		93.113	1075.733061	85.538	122.373	315.635
			±	0.014	0.000031	0.014	0.118	0.220
This work	2009-01-01.0 UTC			315.642	1075.733079	85.420	122.322	315.642
			±	0.014	0.000011	0.081	0.040	0.014
Galatea								
O 1991 [6]	1989-08-18.5 TDB	0.200		46.644	839.659800	46.845	78.167	340.403
			±	0.011	0.002500	0.011	9.470	17.689
JO 2004 [5]	1989-08-18.5 TDB	352.424		54.488	839.661288	46.912	83.871	350.999
			±	0.010	0.000022	0.010	0.084	0.156
This work	2009-01-01.0 UTC			351.114	839.661311	46.865	83.911	351.114
			±	0.008	0.000005	0.035	0.018	0.008
Larissa								
O 1991 [6]	1989-08-18.5 TDB	0.197		184.828	649.053400	185.025	359.304	42.854
			±	0.009	0.001600	0.009	6.061	11.321
JO 2004 [5]	1989-08-18.5 TDB	352.424		192.665	649.054076	185.090	1.929	47.701
			±	0.008	0.000013	0.008	0.050	0.092
This work	2009-01-01.0 UTC			47.807	649.054085	185.133	2.006	47.807
			±	0.006	0.000004	0.026	0.013	0.006

			As Published		1989-08-18.5 TDB	2000-01-01.5 TDB	2009-01-01.0 UTC
Orbit & Referen	**Epoch**	**Origin (°)**	**λ (°)**	**n (°/day)**	**λ (°)**	**λ (°)**	**λ (°)**
Proteus							
O 1991 [6]	1989-08-18.5 TDB	0.136	213.669	320.765400	213.805	273.140	349.639
			± 0.007	0.000900	0.007	3.409	6.368
JO 2004 [5]	1989-08-18.5 TDB	352.424	221.446	320.765626	213.870	274.061	351.303
			± 0.006	0.000005	0.006	0.020	0.036
J 2009 [4]	2000-01-01.5 TDB	−0.037	274.037	320.765625	213.814	274.000	351.236
This work	2009-01-01.0 UTC		351.307	320.765625	213.880	274.068	351.307
			± 0.002	0.000001	0.009	0.005	0.002

The mean longitude of each Voyager-discovered moon is propagated to the epoch of each published solution. All are referenced to the zero longitude as defined in the Methods section. The origin column indicates the location in this frame of the published reference longitude used for that orbit; it must be added to the published solution to match the frame defined herein. Quoted uncertainties are ± 1σ.

Extended Data Table 4 |

Candidate Voyager images of Hippocamp

Image	*X* (sample)	*Y* (line)	Inside?	Exposure Time (s)	Phase Angle (°)	Range (km)
C1120426.IMG	996	−120	no	2.88	14.875	8,994,200
C1121132.IMG	970	242	no	61.44	14.382	8,772,700
C1121139.IMG	955	255	no	61.44	14.386	8,769,200
C1121214.IMG	925	823	no	61.44	14.412	8,751,400
C1121221.IMG	906	835	no	61.44	14.419	8,747,700
C1121346.IMG	570	434	yes	61.44	14.530	8,700,300
C1121353.IMG	543	441	yes	61.44	14.541	8,696,100
C1121428.IMG	458	985	no	61.44	14.603	8,674,400
C1121435.IMG	428	990	no	61.44	14.617	8,669,900
C1121741.IMG	672	403	yes	61.44	15.045	8,529,400
C1121744.IMG	658	400	yes	61.44	15.053	8,526,800
C1121747.IMG	57	394	yes	61.44	15.060	8,524,200
C1121750.IMG	43	391	yes	61.44	15.068	8,521,600
C1121802.IMG	536	999	no	61.44	15.098	8,510,900
C1121805.IMG	−27	992	no	15.36	15.106	8,507,800
C1121808.IMG	−40	989	no	15.36	15.114	8,505,100
C1131016.IMG	−176	−94	no	15.36	16.292	3,940,700
C1133210.IMG	957	372	no	3.84	15.039	2,981,700
C1133624.IMG	813	101	no	3.84	16.589	2,719,300
C1133630.IMG	781	59	yes	3.84	16.613	2,712,500

X (“sample”) and *Y* (“line”) are pixel coordinates, where (1,1) refers to the middle of the upper left pixel and Y is measured downward; this is the convention for the Voyager camera. Predicted coordinates do not account for the innate distortion or the pointing uncertainties of the Voyager images. “Inside?” is “yes” if both of Hippocamp’s coordinates fall inside the range 1–800, which indicates that Hippocamp is more likely to fall inside the field of view.

Supplementary Material

Refer to Web version on PubMed Central for supplementary material.

Acknowledgments

Support for this work was provided by NASA through grant numbers HST-GO-10398, 11656, and 14217 from the Space Telescope Science Institute, which is operated by AURA, Inc., under NASA contract NAS 5–26555. Additional support for MRS and RSF was provided by NASA's Outer Planets Program through grant NNX14AO40G.

We thank Anthony Roman of Space Telescope Science Institute for his extensive support during the planning of the HST observations. Marina Brozovic of JPL provided numerical integrations to help us identify detections of Naiad.

References

1. Smith BA, Soderblom LA, Banfield D, Barnet C et al. Voyager 2 at Neptune: Imaging Science results. Science 246, 1422–1449 (1989). [PubMed: 17755997]
2. Colwell JE & Esposito LW Origins of the Rings of Uranus and Neptune 1. Statistics of Satellite Disruptions. J. Geophys. Res 97, 10,227–10,241 (1992).
3. Banfield D & Murray N A dynamical history of the inner Neptunian satellites. Icarus 99, 390–401 (1992).
4. Showalter MR, de Pater I, Lissauer JJ & French RS NEW SATELLITE OF NEPTUNE: S/2004 N 1. CBET 3586 (2013).
5. Jacobson RA The orbits of the Neptunian satellites and the orientation of the pole of Neptune. Astron. J 137, 4322–4329 (2009).
6. Jacobson RA & Owen WM The orbits of the inner Neptunian satellites from Voyager, Earth-based, and Hubble Space Telescope observations. Astron. J 128, 1412–1417 (2004).
7. Owen WM, Vaughan RM & Synnott SP Orbits of six new satellites of Neptune. Astron. J 101, 1511–1515 (1991).
8. Marchis F, Urata R, de Pater I, Gibbard S, Hammel HB & Berthier J Neptunian satellites observed with Keck AO system. Bull. Amer. Astron. Soc 36, 860 (2004).
9. Brozovic M, Showalter MR, Jacobson RA, French RS, de Pater I & Lissauer J Orbits of the inner satellites of Neptune. AAS/DDA meeting #49, 402.01 (2018).
10. Thomas P & Veverka J Neptune's small, inner satellites. J. Geophys. Res 96, 19,261–19,268 (1991).
11. Karkoschka E Sizes, shapes, and albedos of the inner satellites of Neptune. Icarus 162, 400–407 (2003).
12. Showalter MR & Hamilton DP Resonant interactions and chaotic rotation of Pluto's small moons. Nature 522, 45–49 (2015). [PubMed: 26040889]
13. Croft SK Proteus: Geology, Shape, and Catastrophic Disruption. Icarus 99, 402–419 (1992).
14. Greenzweig Y & Lissauer JJ Accretion rates of protoplanets. Icarus 87, 40–77 (1990).
15. Zhang K & Hamilton DP Orbital resonances in the inner Neptunian system II. Resonant history of Proteus, Larissa, Galatea, and Despina. Icarus 193, 267–282 (2008).
16. Tittemore WC, & Wisdom J Tidal Evolution of the Uranian Satellites. Icarus 85, 394–443 (1990).
17. Krist J & Hook R The Tiny Tim User's Guide Version 6.3. http://tinytim.stsci.edu/static/tinytim.pdf (2004).
18. Renner S & Sicardy B Use of the geometric elements in numerical simulations. Celestial Mech. Dyn. Astron 94, 237–248 (2006).
19. Shupe DL & Hook RN The SIP Convention for Representing Distortion in FITS Image Headers. ASP Conference Series XXX, P3.2.18 (2005).
20. Showalter MR & Lissauer JJ The second ring-moon system of Uranus: Discovery and dynamics. Science 311, 973–977 (2006). [PubMed: 16373533]

21. Dressel L Wide Field Camera 3 Instrument Handbook, Version 10.0, STScI, Baltimore (2018). http://www.stsci.edu/hst/wfc3/documents/handbooks/currentIHB/wfc3_cover.html.

22. Bohlin RC Perfecting the Photometric Calibration of the ACS CCD Cameras. Astron. J 152, 60 (2016).

23. Beers TC, Flynn K, & Gebhardt K Measures of Location and Scale for Velocities in Clusters of Galaxies—A Robust Approach. Astron. J 100, 32–49 (1990).

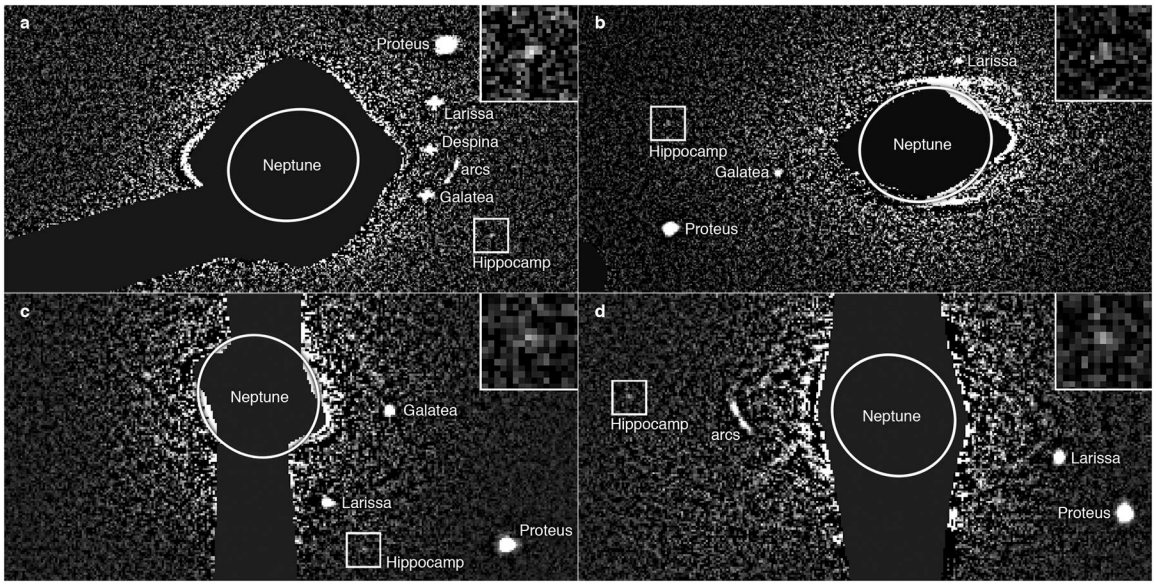

Fig. 1 |. Detections of Hippocamp 2004–2016.

a, View from Visit 04 of GO-10398, showing the earliest detection on 2004 December 9. Neptune is behind the HRC occulting mask. **b**, Visit 08, GO-10398, 2005 May 12. **c**, View from the first orbit from Visit 01, GO-11656, 2009 August 19. The gray vertical band is due to Neptune's saturation bloom. **d**, Visit 03, GO-14217, 2016 September 2. Panels **a** and **b** have been rotated 90° counterclockwise. A small square locates Hippocamp in each panel; a closeup is inset at upper right. Other moons and the outline of Neptune are identified.

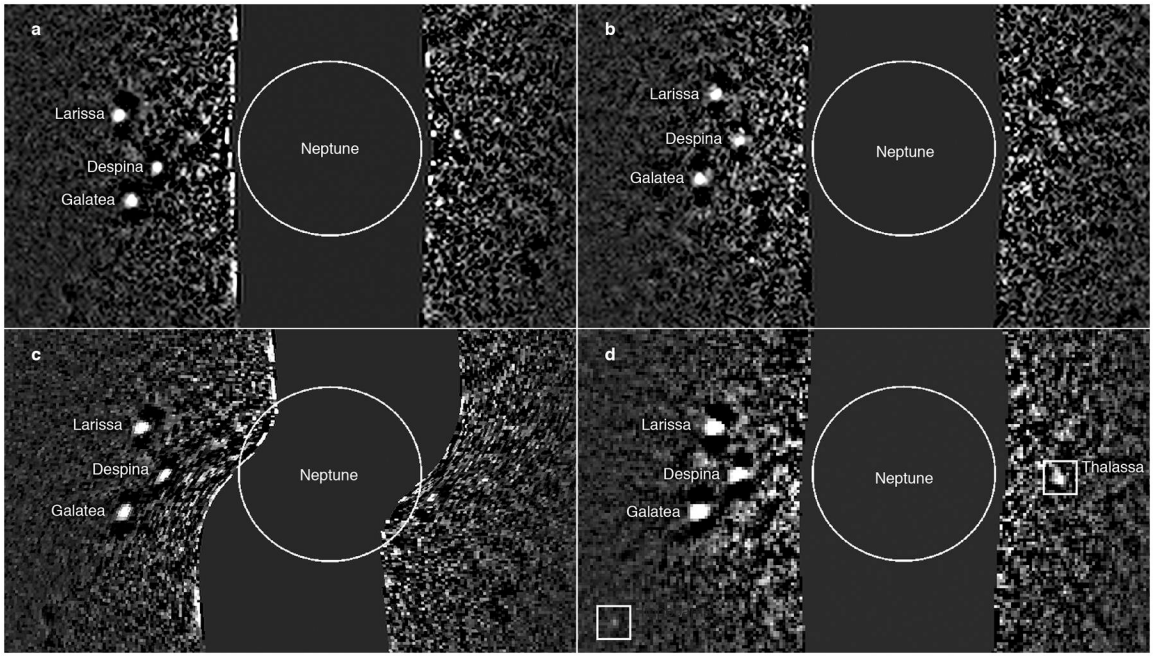

Fig. 2 |. Image processing steps leading to the discovery of Hippocamp.

a, Image ib2e02ziq_flt, the first in a sequence of eight long exposures from the second HST orbit of Visit 02 in program GO-11656 (2009 August 19). **b**, Image ib2e02zmq_flt, taken 21 minutes later. Despina, Galatea, and Larissa have shifted noticeably in position. **c**, Image from panel **a**, transformed to match the geometry of the image in panel **b**. **d**, The result of coadding all eight images, revealing Hippocamp and Thalassa. The outline of Neptune's disk, as distorted by the camera, is shown in each panel.

Table 1 |

Properties of Neptune's moons from HST data 2004–2016

	Naiad	Thalassa	Despina	Galatea	Larissa	Hippocamp	Proteus	Triton
n **(°/day)**	1,222.858303	1,155.758516	1,075.733079	839.661311	649.054085	378.906246	320.765625	−61.257264
±	0.000133	0.000033	0.000011	0.000005	0.000004	0.000025	0.000001	
a **(km)**	48,224	50,074	52,526	61,953	73,548	105,284	117,647	354,759
a **(R_N)**	1.9118	1.9851	2.0823	2.4560	2.9157	4.1738	4.6639	14.0638
e	0.00342	0.00224	0.00050	0.00022	0.00118	0.00048	0.00044	0.00034
±	0.00132	0.00056	0.00015	0.00008	0.00005	0.00032	0.00002	0.00007
i **(°)**	5.0733	0.1371	0.0583	0.0231	0.1880	0.0641	0.0478	23.0965
±	0.1723	0.0693	0.0146	0.0091	0.0058	0.0507	0.0025	0.0079
λ_0 (°)	156.354	50.874	315.642	351.114	47.807	325.108	351.307	−24.050
±	0.248	0.077	0.014	0.008	0.006	0.044	0.002	0.006
ϖ_0 (°)	317.200	229.884	214.655	225.806	44.434	3.408	269.777	100.587
±	22.709	14.362	17.303	19.789	2.590	42.231	2.905	9.602
Ω_0 (°)	164.507	225.730	244.989	196.943	99.258	32.855	47.051	2.528
±	1.962	28.964	13.846	18.677	1.707	41.595	2.999	0.031
ϖ' (°/day)	1.694327	1.507828	1.274838	0.714282	0.391340	0.111343	0.075456	−0.001097
Ω' (°/day)	−1.711963	−1.505878	−1.273331	−0.713675	−0.391111	−0.111311	−0.075448	0.001434
ψ (°)	0.0054	0.0066	0.0085	0.0198	0.0480	0.3078	0.5483	0.0000
N_1	16	46	225	314	346	16	396	36
N_0	0	5	11	6	6	3	11	2
DOF	26	86	444	622	686	26	786	67
GOF	1.19	1.41	1.02	0.95	0.97	1.23	0.89	0.73
RMS (″)	0.013	0.010	0.012	0.010	0.008	0.007	0.004	0.007
D **(km^2)**	404.5	598.8	1,516	2,262	2,254	86.0	11,745	
±	56.5	78.1	327	266	127	17.1	749	
R **(km)**	37.8	46.0	73.2	89.4	89.3	17.4	203.8	
±	3.4	3.9	8.9	7.2	5.6	2.0	13.1	

R_N is the radius of Neptune, 25,225 km; N_1 and N_0, are the number of weighted and unweighted measurements, respectively; DOF = degrees of freedom; GOF = goodness of fit, equal to $(\chi^2/\mathrm{DOF})^{1/2}$; RMS = the root-mean-square residual of the measurements from the orbit model. Uncertainties are one standard deviation. Longitudes are measured from the ascending node of the Neptune system's invariable plane on the ICRF equator; see the Methods section. For Triton, angles are measured in the prograde direction but motions are sign-reversed. The epoch is 2009 January 1 UTC. Note that Triton's *a*, *n*, and Ω' were held fixed in this analysis[5,6].